Supporting Information

3D-Hierarchical Porous Nickel Sculptured by a Simple Redox Process and Its Application for High-Performance Supercapacitor

Zhihong Wang*, Yingming Yan, Yifu Chen, Wenqiao Han, Mengting Liu, Kongfa Chen, Yaohui Zhang, Xingbao Zhu, Bo Wei, Xiqiang Huang, Yueping Xiong, Zhe Lv* and Meilin Liu*

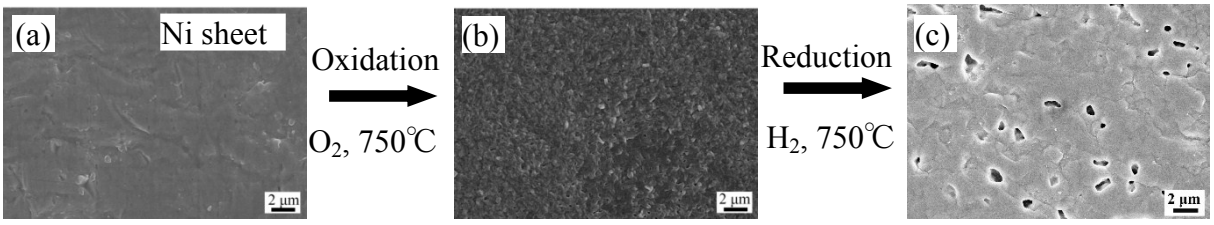

Fig. S1 SEM images of the surface morphologies of Ni sheets. (a) Fresh Ni sheet, (b) after oxidation in pure O_2 for 1 h, and (c) after subsequent reduction in H_2 for 2 h at 750 ℃. A large number of NiO grains grew out of the surface of Ni sheet during the oxidation process, coarsening the surface, while after reduction the surface NiO grains disappeared and some pores were observed, owing to the volume reduction and reconstruction of Ni metal atoms under this operating condition.

.

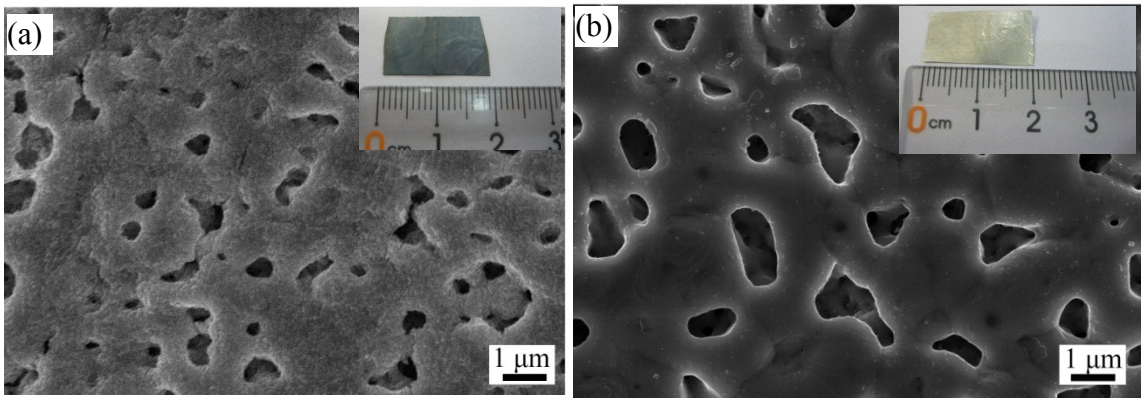

Fig. S2 SEM images of the top views of Ni sheets. (a) After redox treatment in CH_4-O_2 mixed gas for 5 h at 750 ℃ and (b) after subsequent reduction in H_2. Insets are the corresponding optical images. When a Ni sheet was redox treated in CH_4-O_2 mixture for 5 h, its color was changed from white to black (see the inset in (a)). The SEM observations revealed that although some cavities were formed, their surfaces were rough with small particles, similar to the observation on the Ni sheet after oxidation (Fig. S1), implying the presence of NiO grains. After reduction in H_2, the Ni metal was recovered to its original color in (b) and its surface became smooth.

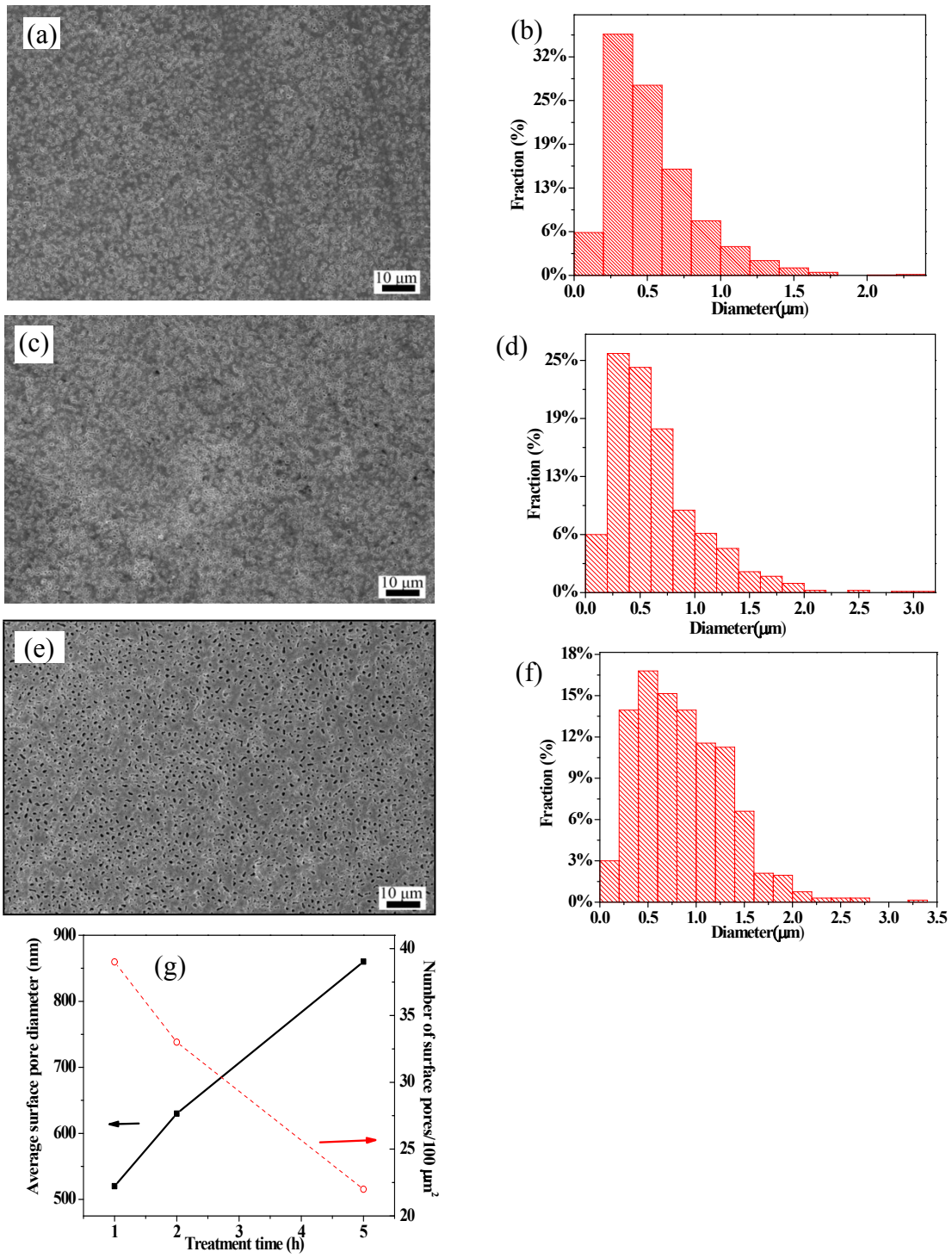

Fig. S3 (a, c, e) SEM images of the top views of Ni sheets after exposure in CH_4-O_2 at 750 ℃ for 1, 2 and 5 h. These low magnification images are related to those shown in Fig. 2c-f. (b, d, f) The diameter distribution graph of Ni pores after exposure in CH_4-O_2 at 750 ℃ for 1, 2 and 5 h. (g) The dependence of the average surface pore diameter (solid line) and number of surface pores over an area of 100 μm^2 (dotted line) on the exposure times of CH_4-O_2.

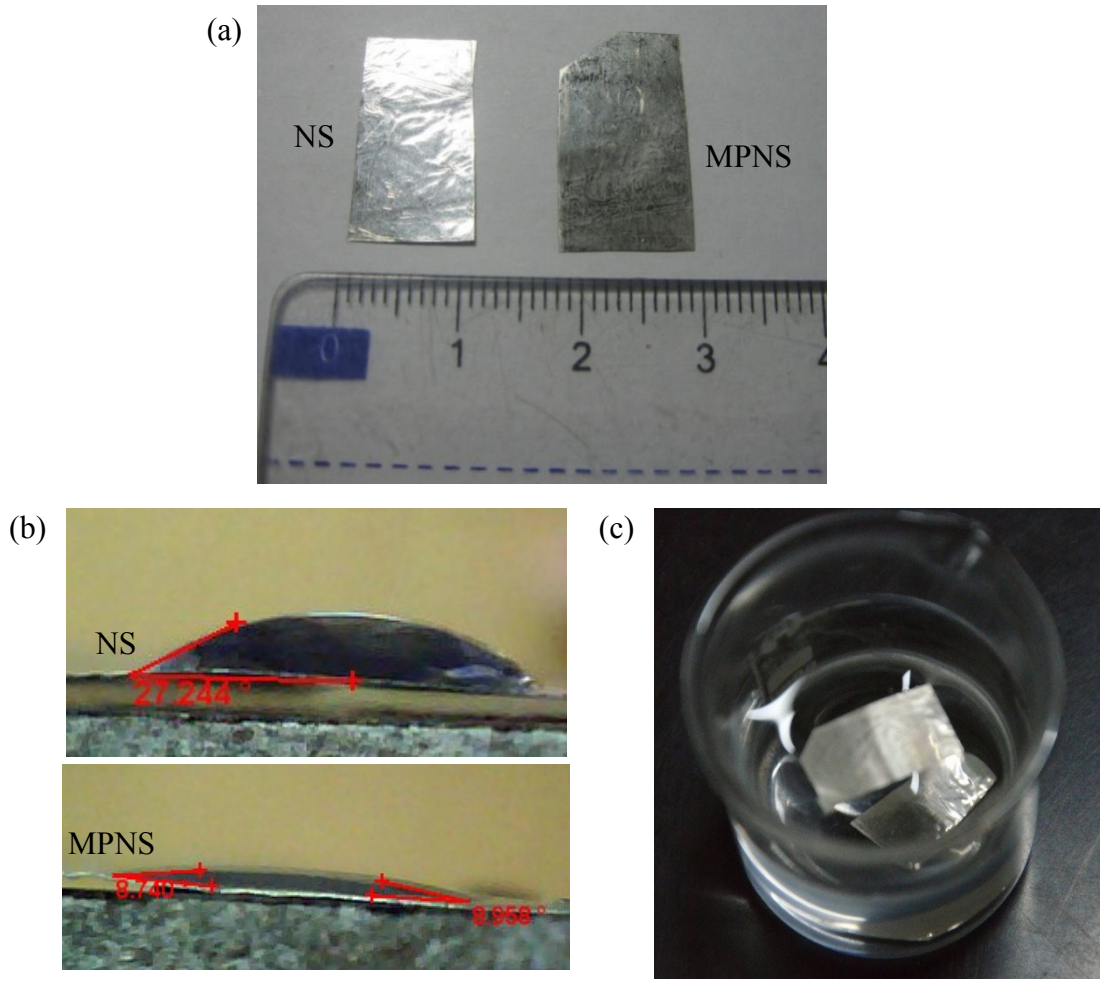

Fig. S4 (a) Optical images of pure Ni sheet (NS) and micron porous Ni sheet (MPNS). (b) Water contact angle measurement on the surfaces of NS and MPNS. The water contact angle of MPNS (8.7^{o}） is smaller than 27.2^{o} of NS, suggesting that MPNS possesses a coarse surface.[1] (c) Float experiment of NS and MPNS.

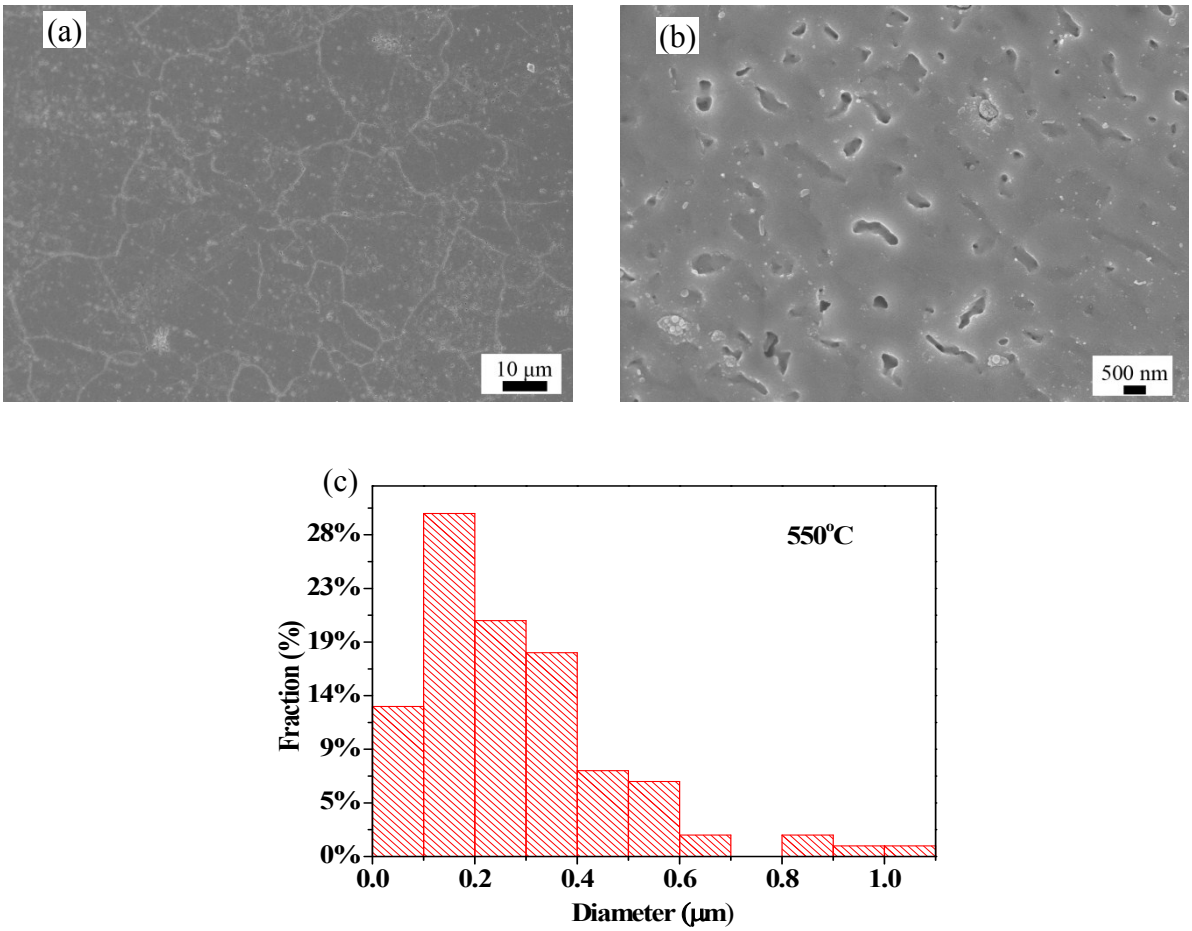

Fig. S5 (a, b) SEM images of the top views of Ni sheets after exposure in CH_4-O_2 at 550 ℃ for 5 h. (c) The diameter distribution graph of Ni pores in Fig. S5(a).

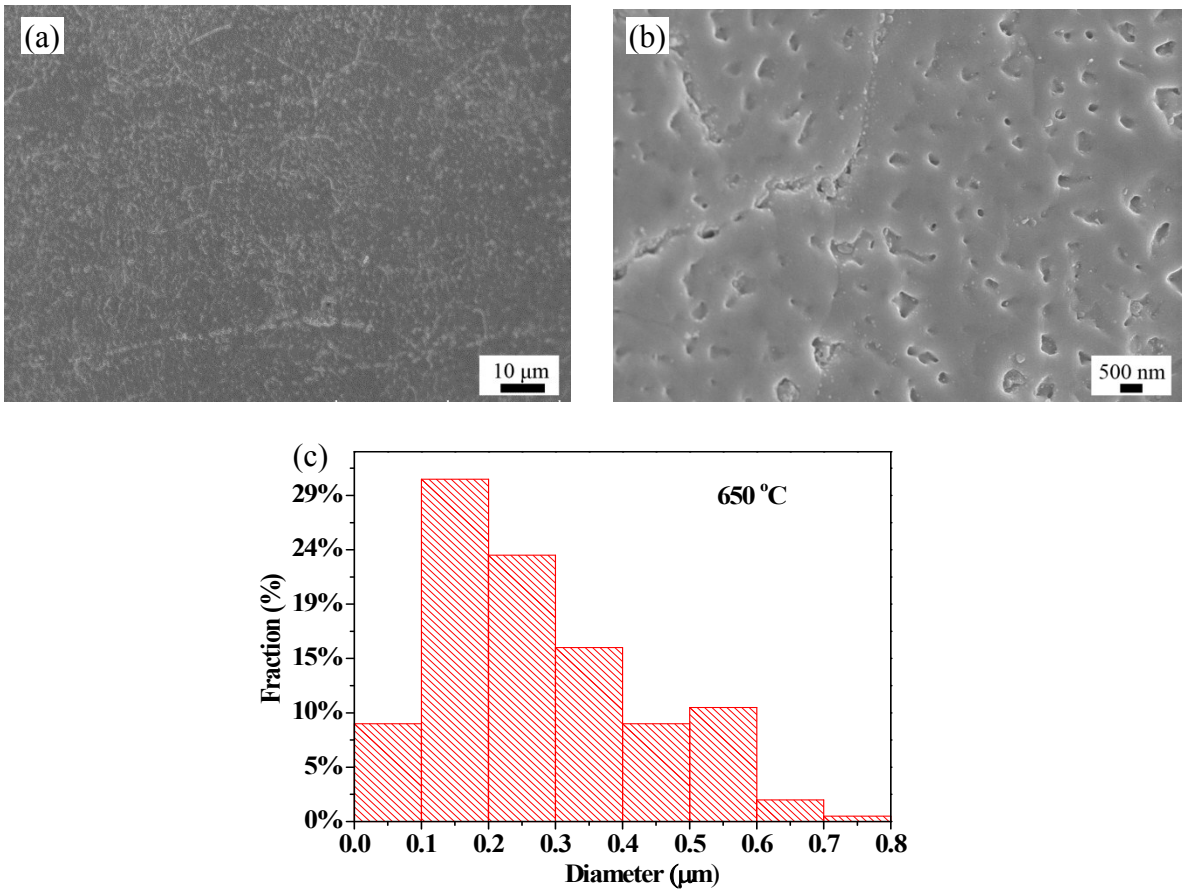

Fig. S6 (a, b) SEM images of the top views of Ni sheets after exposure in CH_4-O_2 at 650 ℃ for 5 h. (c) The diameter distribution graph of Ni pores in Fig. S6(a).

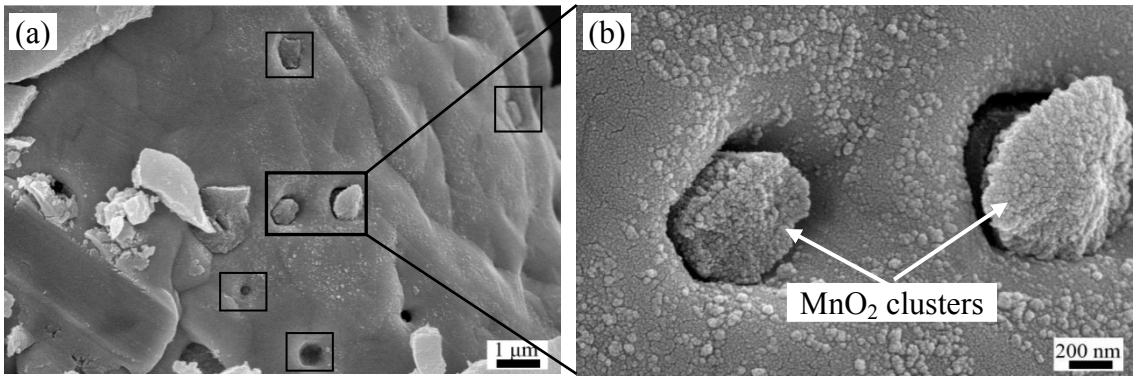

Fig. S7 (a) SEM images of MnO_2 clusters immersed in the micron pores of ligament of MPNF and (b) the magnified image of selected area in (a). In order to observe the distribution of nanocrystalline MnO_2 on the cellular structure of MPNF, the outer layer of MnO_2 film was cleaned up using the ultrasonic method.

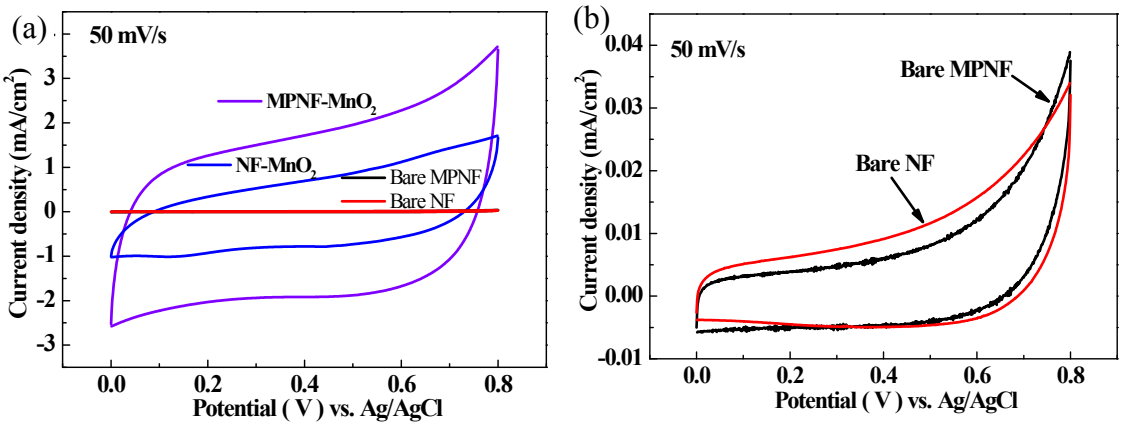

Fig. S8 (a) Cyclic voltammograms of NF/MPNF-supported MnO_2 electrodes and bare NF/MPNF measured between 0 and 0.8V at a scan rate of 50 mV/s. (b) Enlarged view of CV for bare NF and MPNF. Clearly, the peak current density of MPNF-MnO_2 and NF-MnO_2 electrode are ~100 times higher than those of the bare MPNF and NF, indicating the NF and MPNF delivered negligible capacitance.

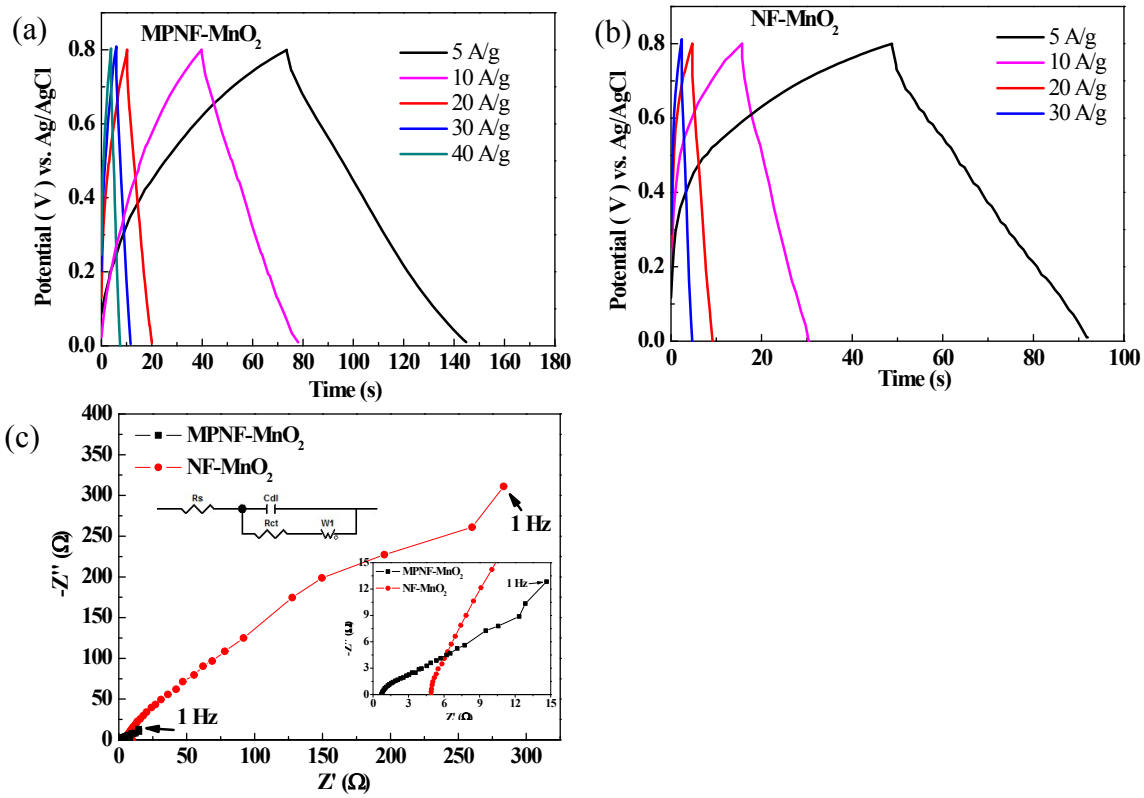

Fig. S9 Gavanostatic charge-discharge curves at different current densities for (a) MPNF-MnO_2 and (b) NF-MnO_2 electrodes (plating time of 5 min). (C) EIS Nyquist plots of MPNF-MnO_2 and NF-MnO_2 electrodes (inserts are magnified EIS curves at high frequency and an equivalent circuit fitting to the EIS curves, respectively).

Table S1. Comparison of the major figures of merits of Ni foam supported MnO_2 electrodes in terms of specific capacitance and cycling performance.

Materials	Specific capacitance (F/g) at given current density (A/g)	Retention after given cycles and current density (A/g)	Ref.
MPNF-MnO_2	478.8 F/g (10 A/g)	121 % (10 A/g, 10,000)	This work
Ni foam-MnO_2	122 F/g (10 A/g)	65% (5 A/g, 1800)	2
Ni foam-ZnO_2-MnO_2	152.2 F/g (10 A/g)	92% (5 A/g, 3000)	3
Ni foam-Carbon nanotubes-MnO_2	230 F/g (10 A/g)	93.5% (10 A/g, 5000)	4
Ni foam- Carbon nanotube-MnO_2	251 F/g (1 A/g)	82% (1.0 A/g, 3000)	5
Ni foam-reduced graphene oxide-MnO_2	267 F/g (0.25 A/g)	89.5% (1 A/g, 1000)	6
Ni foam-reduced graphene oxide-MnO_2	295 F/g (10 A/g)	93.1% (10 A/g, 5000)	7

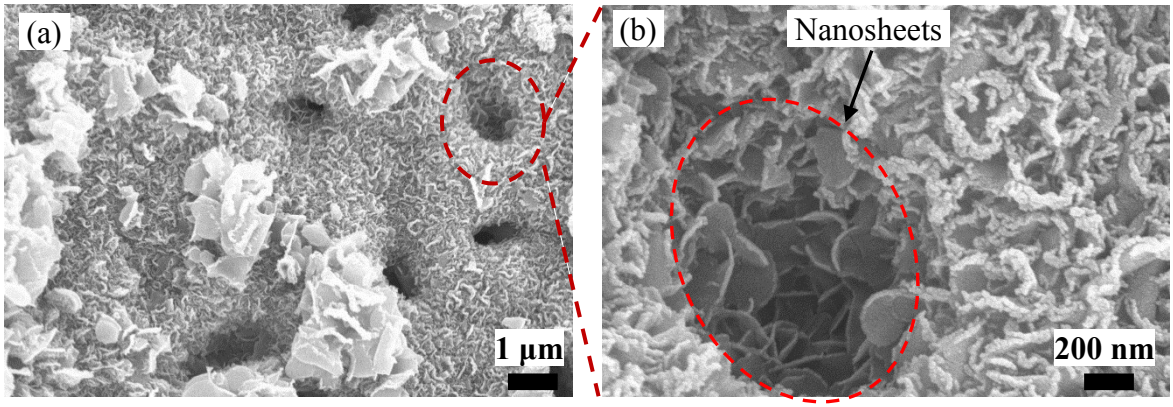

Fig. S10 (a) and (b) Morphology of MPNF-MnO_2 electrode after 10,000 cycles at 10 A/g

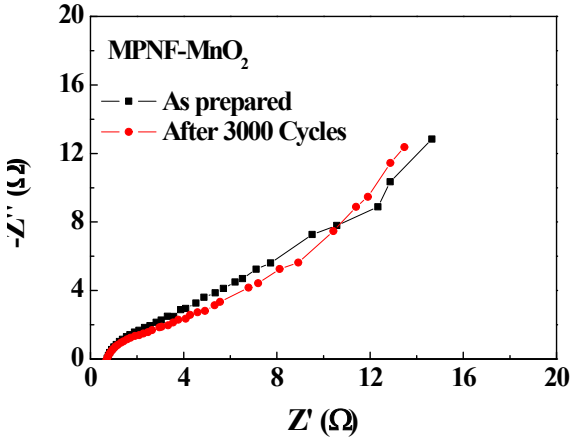

Fig. S11 Nyquist plots of the EIS of the MPNF-MnO_2 electrode before and after 3000 cycles

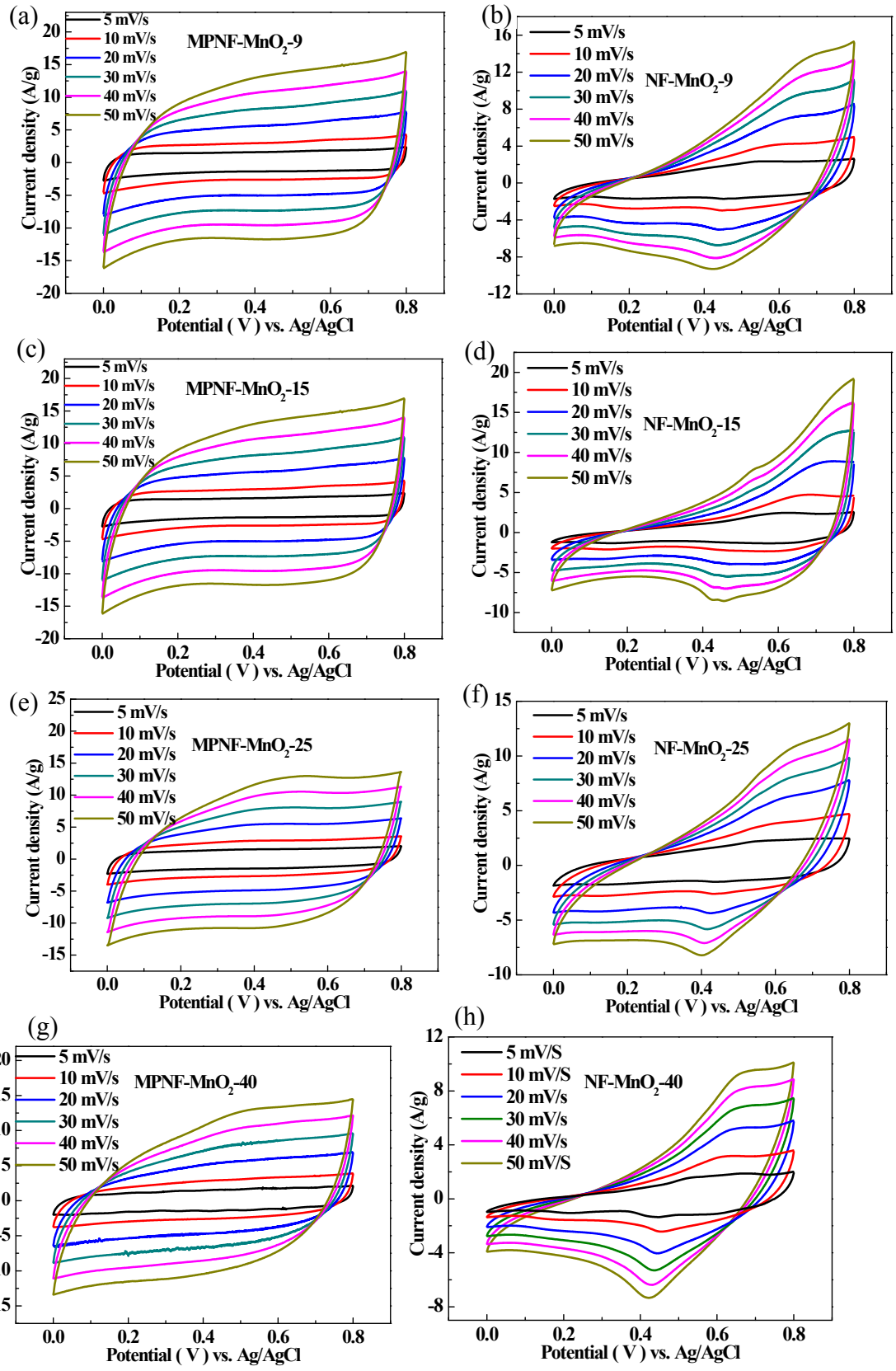
(a)
MPNF-MnO2-9
5 mV/s
10 mV/s
20 mV/s
30 mV/s
40 mV/s
50 mV/s
Current density (A/g)
Potential (V) vs. Ag/AgCl
(b)
NF-MnO2-9
(c)
MPNF-MnO2-15
(d)
NF-MnO2-15
(e)
MPNF-MnO2-25
(f)
NF-MnO2-25
(g)
MPNF-MnO2-40
(h)
NF-MnO2-40
5 mV/S
10 mV/S
50 mV/S

(i)

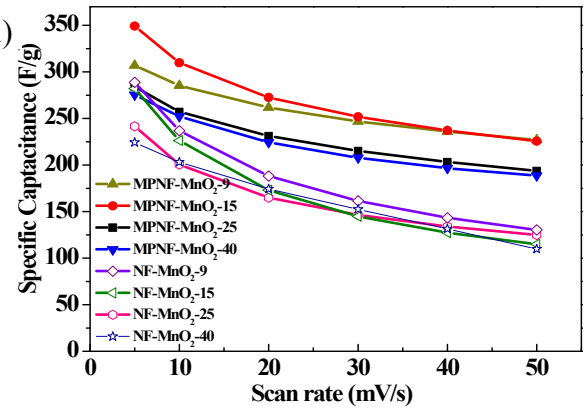

Fig. S12 CV curves at different scan rates for MPNF-MnO_2 electrodes with plating time of (a) 9 min, (c) 15 min, (e) 25 min and (g) 45 min; CV curves at different scan rates for NF-MnO_2 electrodes with plating time of (b) 9 min, (d) 15 min, (f) 25 min and (h) 45 min. (i) Specific capacitances of MPNF-MnO_2 and NF-MnO_2 electrodes versus scan rates for four different plating times.

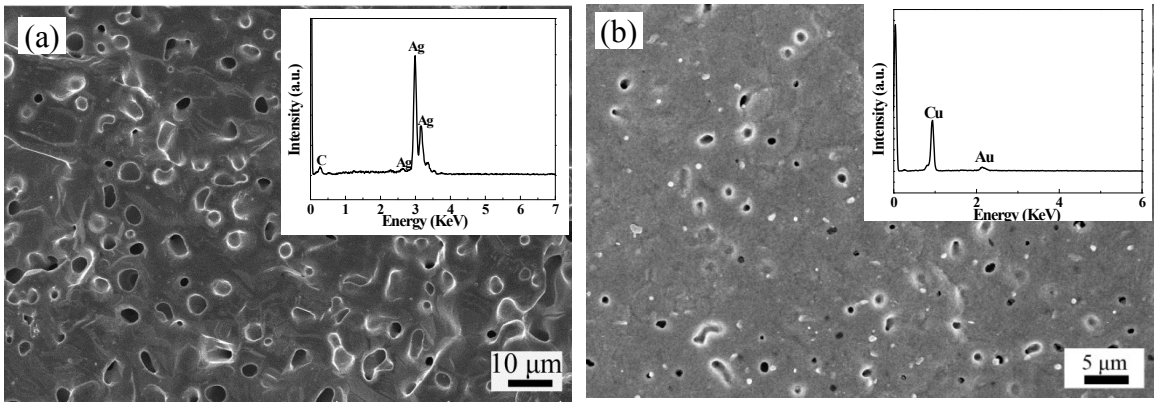

Fig. S13 (a) SEM image of cellular structure of Ag sheet, which is fabricated after exposing to CH_4-O_2 mixed gas for 3 h at 750 ℃with the presence of Ni-yttria-stabilized zirconia (YSZ) catalyst. (b) SEM image of cellular structure of Cu sheet, which is fabricated after exposure to CH_4-O_2 mixed gas for 2 h at 750 ℃with the Ni-YSZ catalyst. Inserts are the EDX spectra of the corresponding Ag and Cu sheets. Taking account of the decomposition of Ag_2O at temperature above 230 ℃, the formation of cellular structure in mixed gas is mainly attributed to simultaneous diffusion of hydrogen, carbon monoxide and oxygen into Ag bulk, followed by subsequent interaction resulting in the formation of water and carbon dioxide gas.[8, 9] However, for Cu metal, the cellular structure also originates from the multiply reduction and oxidation (redox) cycles taking place on its surface.

References:

1 R. Wenzel, *Ind. Eng. Chem. Res.* 1936, 28, 988-994.

2 M. Kundu, L. F. Liu, *J Power Sources*, 2013, 243, 676-681.

3 M. Huang, F. Li, X. L. Zhao, D. Luo, X. Q. You, Y. X. Zhang, G. Li, *Electrochim Acta*, 2015, 152, 172-177.

4 M. Huang, R. Mi, H. Liu, F. Li, X. L. Zhao, W. Zhang, S. X. He, Y. X. Zhang, *J Power Sources*, 2014, 269, 760-767.

5 G. Y. Zhu, Z. He, J. Chen, J. Zhao, X. M. Feng, Y. W. Ma, Q. L. Fan, L. H. Wang, W. Huang, *Nanoscale*, 2014, 6, 1079-1085.

6 Y. J. Li, G. L. Wang, K. Ye, K. Cheng, Y. Pan, P. Yan, J. L. Yin, D. X. Cao, *J Power Source*, 2014, 271, 582-588.

7 Y. J. Li, D. X. Cao, Y. Wang, S. A. Yang, D. M. Zhang, K. Ye, K. Cheng, J. L. Yin, G. L. Wang, Y. Xu, *J Power Sources*, 2015, 279, 138-145.

8 P. Singh, Z. G. Yang, V. Viswanathan, J. W. Stevenson, *J. Mater. Eng. Perform*., 2004, 13, 287-294.

9 N. Akhtar, S. P. Decent, K. Kendall, *Int. J. Hydrogen Energy*, 2009, 34, 7807-7810.